ROYAL SOCIETY
OF CHEMISTRY

PAPER

Check for updates

Facile hydrothermal synthesis of porous MgCo$_2$O$_4$ nanoflakes as an electrode material for high-performance asymmetric supercapacitors†

Huiyu Chen, Xuming Du, Runze Wu, Ya Wang, Jiale Sun, Yanfei Zhang and Chunju Xu (iD) *

In this work, porous MgCo$_2$O$_4$ nanoflakes (MgCo$_2$O$_4$ NFs) and MgCo$_2$O$_4$ nanocubes (MgCo$_2$O$_4$ NCs) have been successfully synthesized through a simple hydrothermal method combined with a post calcination process of the precursor in air. The morphology of the MgCo$_2$O$_4$ samples can be easily tuned by changing the hydrothermal temperature and reaction time, respectively. The porous MgCo$_2$O$_4$ NFs with an average pore size of 12.5 nm had a BET specific surface area up to 64.9 m^2 g^{-1}, which was larger than that of MgCo$_2$O$_4$ NCs (19.8 m^2 g^{-1}). The MgCo$_2$O$_4$ NFs delivered a specific capacitance of 734.1 F g^{-1} at 1 A g^{-1} and exhibited a considerable rate performance with 74.0% capacitance retention at 12 A g^{-1}. About 94.2% of its original capacitance could be retained after 5000 charge–discharge cycles at a constant current density of 5 A g^{-1}. An asymmetric supercapacitor (ASC) was assembled by using MgCo$_2$O$_4$ NFs as the positive electrode and AC as the negative electrode, and the ASC had a wide operation voltage of 1.7 V and a high energy density of 33.0 W h kg^{-1} at a power density of 859.6 W kg^{-1}. Such outstanding electrochemical performances make the MgCo$_2$O$_4$ NFs a promising candidate for supercapacitor applications. In addition, the simple and scalable synthesis method can be extended to the preparation of other metal oxide-based electrode materials.

1. Introduction

The energy crisis and environmental pollution have become more serious in recent years, and so making use of clean and sustainable energies such as solar power, wind energy and bio-fuel is an important issue. Various energy storage and conversion systems with high performance and environmental friendliness have been developed so far. For example, lithium-ion batteries, fuel batteries, supercapacitors, and so on have received increasing attention.[1–3] Among them, supercapacitors have attracted tremendous interest due to their merits of low cost, long cycling stability, fast charge rate, and high power density. With the development of new technology for materials synthesis and device assembly, the performances of supercapacitors have been improved rapidly and they have been applied in a wide range of fields such as hybrid electric vehicles, memory backup systems, emergency lighting systems, and portable military devices.[4,5] However, the relatively low energy density of supercapacitors compared with that of lithium-ion batteries is a serious problem, which may hinder their further applications. It is widely known that the electrode material is a key component in supercapacitors and determines the electrochemical performance to a certain extent.[6,7] The supercapacitors with excellent performance usually possess the characteristics of high specific capacitance and rate capability, long-life cycling stability, and high energy density. It should be noted that these features are closely associated with the specific surface area, electronic/ionic conductivity, and mechanical stability of electrode materials.[8,9] Large specific surface area can provide more active sites for redox reactions, and superior electronic/ionic conductivity ensures that redox reactions can proceed quickly at high current density or scan rate. In addition, good mechanical stability is helpful for the electrode material to retain its structural integrity during the long-term cycling process.

According to the energy storage mechanism, supercapacitors can be divided into two categories including electric double-layer capacitors (EDLCs) and pseudo-capacitors (PCs). EDLCs store charges by ion accumulation at the interface between the electrode material and electrolyte, which is a pure physical process. Carbonaceous materials with large specific surface area, such as activated carbon, graphene, and carbon nanotubes (CNTs), are ideal candidates of electrode materials for EDLCs.[10,11] PCs store energy through reversible faradaic reactions using metal oxides or conducting polymers as common electrode materials. Such energy storage behavior is observed in many chemical reactions, so it is a chemical process. In general,

School of Materials Science and Engineering, North University of China, Taiyuan 030051, China. E-mail: chunju@nuc.edu.cn

PCs can deliver higher specific capacitance and energy density than EDLCs.[12–15] Among the various electrode materials for PCs, transition metal oxides (TMOs) such as NiO, MnO_2 and Co_3O_4 are considered as the most promising candidates owing to their high theoretical specific capacitance.[16] Co_3O_4 can provide relatively huge capacitance owing to its rich redox reactions. However, cobalt is rare in nature and expensive, and such situation may hinder its wide applications in the field of energy storage. A possible and effective method to change this is to partially replace cobalt cations in the Co_3O_4 crystal structure with other cheap metals such as Mg, Mn, Cu, Fe, Ni, Zn, etc.[17] The formed cobalt-based binary transition metal oxides (BTMOs) may have better electrical conductivity and superior electrochemical performances than pure Co_3O_4 owing to the synergistic effect between different metallic ions.[18] For instance, $NiCo_2O_4$ nanowires (NWs) and Co_3O_4 NWs were synthesized by the microemulsion technique combined with a post thermal treatment, and under the same current density of 0.5 A g^{-1}, the specific capacitances could reach 1481 and 990 F g^{-1}, respectively.[19] Another example is $ZnCo_2O_4$ nanoflakes, which could deliver a specific capacitance up to 1220 F g^{-1} at 2 A g^{-1}, which was about 500 F g^{-1} higher than that of Co_3O_4 under the same conditions.[20]

$MgCo_2O_4$ with a spinel structure stands out among a variety of BTMOs because of its high theoretical specific capacitance ($\sim$3122 F g^{-1}) and other good electrochemical properties. In the $MgCo_2O_4$ crystal structure, the Mg cation occupies the tetrahedral site and the Co cation occupies the octahedral site. When used as an electrode material for supercapacitors, elemental Mg does not participate in the redox reactions, and all the reactions come from cobalt with various valence states. However, the magnesium has better conductivity than cobalt, and the specific capacitance of Co_3O_4 is expected to improve if one of the Co cations is replaced by Mg. In other words, $MgCo_2O_4$ probably exhibits better electrochemical performance than Co_3O_4 in practical applications. Several studies focused on the synthesis of $MgCo_2O_4$ with novel morphologies such as submicron prisms,[21] NWs,[22] and nanoneedles[23] have been reported. Typically, the $MgCo_2O_4$ particles synthesized by the molten salt method exhibited a specific capacitance of only 321 F g^{-1} at a current density of 0.5 A g^{-1}.[24] Krishnan et al. reported that $MgCo_2O_4$ cuboidal microcrystals had a capacity of $\sim$345 C g^{-1} at 1 A g^{-1}.[25] A double-urchin-like $MgCo_2O_4$ microstructure was hydrothermally prepared, and it delivered a specific capacitance of 508 F g^{-1} at 2 A g^{-1}.[26] Powdered $MgCo_2O_4$ electrode materials usually have lower specific capacitance than the theoretical value due to the use of binder reagents in the electrode fabrication process, and the structural integrity of the electrode materials often cannot be totally preserved under pressure.[27] Improving the electrochemical performance of $MgCo_2O_4$ has become an urgent issue, and has greatly accelerated the research progress on binder-free synthesis or formation of $MgCo_2O_4$-based composites. For example, nickel foam supported $MgCo_2O_4$ nanocone arrays were directly obtained through a one-step hydrothermal method, and such electrode delivered a capacitance of 750 F g^{-1} at 1 A g^{-1}.[28] The specific capacitance of the $MgCo_2O_4$@ppy urchin-like core–shell

structure could reach 1079.6 F g^{-1} at 1 A g^{-1}, which was mainly contributed by the synergistic effect between $MgCo_2O_4$ and ppy.[29] Gao et al. prepared a $MgCo_2O_4$@$NiMoO_4$ composite with a double-urchin-like hierarchical shape on nickel foam through two-step hydrothermal reactions, and such composite delivered a specific capacitance of 1775 F g^{-1} at 1 A g^{-1} as well as an energy density of 37.5 W h kg^{-1} at a power density of 480 W kg^{-1}.[30] Although research on $MgCo_2O_4$ as an electrode material and its applications in supercapacitors has achieved considerable progress, the specific capacitance is still far below the theoretical value. As for the formation of $MgCo_2O_4$-based composites, the preparation process is generally complicated and not suitable for mass production. Therefore, it is still a big challenge to improve the electrochemical performances of $MgCo_2O_4$ under the premise of easy synthetic operation, large-scale production and low cost.

Herein, we propose a facile hydrothermal method accompanied by a post annealing process to synthesize porous $MgCo_2O_4$ nanoflakes ($MgCo_2O_4$ NFs). To the best of our knowledge, powdered $MgCo_2O_4$ electrode materials with similar shapes have rarely been reported so far. Such porous $MgCo_2O_4$ NFs delivered a specific capacitance of 734.1 F g^{-1} at 1 A g^{-1} and still retained 543.4 F g^{-1} even at a high current density of 12 A g^{-1}. In addition, about 94.2% of the original capacitance was retained after 5000 continuous charge–discharge cycles at 5 A g^{-1}, suggesting the excellent cycling stability of the $MgCo_2O_4$ NF-modified electrode. For comparison, porous $MgCo_2O_4$ nanocubes ($MgCo_2O_4$ NCs) were also hydrothermally prepared at 150 °C while the other synthetic conditions remained the same. The $MgCo_2O_4$ NC-based electrode exhibited a specific capacitance of 541.0 F g^{-1} at 1 A g^{-1} and 440.9 F g^{-1} at 12 A g^{-1}, and the two values were lower than those of $MgCo_2O_4$ NFs, respectively. Furthermore, an asymmetric supercapacitor (ASC) was fabricated by using activated carbon (AC) as the negative electrode and $MgCo_2O_4$ as the positive electrode, respectively. The $MgCo_2O_4$ NFs//AC ASC exhibited higher specific capacitance and energy density than the $MgCo_2O_4$ NCs//AC ASC. Such results illustrate that the $MgCo_2O_4$ NFs have excellent electrochemical performance and can serve as a promising electrode material for energy storage in the future.

2. Experimental section

2.1. Materials and methods

All reagents used in this work were of analytical grade and were used directly without extra purification. In a typical synthesis, 0.214 g of $(CH_3COO)_2Mg \cdot 4H_2O$, 0.498 g of $(CH_3COO)_2Co \cdot 4H_2O$ and 0.6 g urea were dissolved in 40 mL of distilled water with magnetic stirring. Then, the obtained solution was transferred into a 50 mL Teflon-lined stainless-steel autoclave, sealed, and maintained at 120 °C for 10 h in an electric oven. After cooling down to room temperature naturally, the precipitate was collected by centrifugation, rinsed several times with distilled water and absolute ethanol, respectively, and then dried at 60 °C. Finally, the powdered precursor was calcined at 400 °C for 3 h with a ramp rate of 5 °C min^{-1}.

2.2. Characterization

The XRD pattern was collected on a powder X-ray diffractometer (XRD, Bruker D8 Advance) using a Cu-Kα ($\lambda = 0.1548$ nm) X-ray source and the 2θ value ranged from 10 to 70°. The morphology of the sample was observed under a field-emission scanning electron microscope (FESEM, JEOL JSM7100F). The transmission electron microscopy (TEM) image, high-resolution TEM (HRTEM) image and selected-area electron diffraction (SAED) pattern were obtained using a transmission electron microscope (JEOL JEM2100F) with an accelerating voltage of 200 kV. In order to perform the TEM characterization, the sample was dispersed in absolute ethanol and then dropped onto a carbon-coated copper mesh. The surface chemical composition and elemental valence states were investigated by X-ray photoelectron spectroscopy (XPS), which was performed on an ESCALAB 250 spectrometer using an Al Kα (1486.6 eV) X-ray source. N_2 adsorption–desorption isotherms were obtained on a Quantachrome Autosorb 1-C adsorption analyzer at 77 K to evaluate the porous structure including the specific surface area, average pore size and pore distribution, which were analyzed by using the Brunauer–Emmett–Teller (BET) and Barrett–Joyner–Halenda (BJH) methods, respectively.

2.3. Electrochemical tests

The working electrode was fabricated as follows. The active material, conductive acetylene black and polyvinylidene fluoride (PVDF) binder with a mass ratio of 80 : 15 : 5 were mixed and dispersed in N-methyl-2-pyrrolidone (NMP) solvent, then the resulting slurry was coated on nickel foam with a loading area of about 1×1 cm^2. After drying at 95 °C in a vacuum oven, the nickel foam with loaded $MgCo_2O_4$ (2.0 mg for NFs and 2.1 mg for NCs) was pressed under a pressure of 10 MPa. All the electrochemical tests including cyclic voltammetry (CV), galvanostatic charge–discharge (GCD), electrochemical impedance spectroscopy (EIS), and cycling were carried out on a CHI 660E electrochemical workstation (Shanghai Chenhua Instrument Co., China). The measurements were performed in a typical three-electrode system using 2 M KOH aqueous solution as the electrolyte, and Pt wire and a saturated calomel electrode (SCE) as the counter and reference electrodes, respectively. The potential window for CV measurements was fixed at 0–0.6 V and the scan rate increased from 5 to 50 mV s^{-1}. The GCD tests were carried out within a potential window of 0–0.43 V while the current density varied in the range of 1–12 A g^{-1}. Under an open circuit potential with an AC amplitude of 5 mV, the EIS test was performed in the frequency range of 10^5 to 10^{-2} Hz. In addition, 2 M KOH aqueous solution was also used as an electrolyte for the two-electrode tests. The ASC was assembled by using activated carbon (AC) as the negative electrode and $MgCo_2O_4$ as the positive electrode, respectively.

According to the GCD curves, the specific capacitance, energy density and power density of the $MgCo_2O_4$ electrode material can be calculated based on the following equations:

$$C = I\Delta t/m\Delta V \quad (1)$$

$$E = C\Delta V^2/7.2 \quad (2)$$

$$P = 3600E/\Delta t \quad (3)$$

where C (F g^{-1}) is the specific capacitance, Δt (s) indicates the discharge time, I (A) represents the discharge current, m (g) is the mass of the active material, ΔV (V) is the potential window, and E (W h kg^{-1}) and P (W kg^{-1}) represent the energy density and power density, respectively. As for the tests in the two-electrode system, m (g) indicates the total mass of active materials within both the negative and positive electrodes.

3. Results and discussion

The composition of the precipitate after hydrothermal reaction was investigated by XRD, and the typical XRD pattern is presented in the ESI (Fig. S1).† The precursor contained Mg_2-$CO_3(OH)_2 \cdot 0.5H_2O$ (JCPDS no. 37-0454) and $Co(CO_3)_{0.5}(OH) \cdot 0.11H_2O$ (JCPDS no. 48-0083). After thermal treatment of the precursor at 400 °C for 3 h, the crystal structure and phase purity of the final $MgCo_2O_4$ were also investigated by the XRD technique. As shown in Fig. 1, eight well-defined diffraction peaks were located at 18.8°, 31.5°, 36.9°, 38.3°, 44.9°, 55.4°, 59.2°, and 65.2°, which matched well with previously reported data.[31] Such result demonstrated the cubic spinel structure of $MgCo_2O_4$ (JCPDS no. 81-0667, $a = b = c = 8.10$ Å). All the diffraction peaks were sharp, suggesting good crystallization of the sample. In addition, there were no other peaks ascribed to impurities, revealing high purity of these $MgCo_2O_4$ NFs.

The SEM technique was used to investigate the morphology and size of the obtained product. Fig. 2 presents several SEM images of $MgCo_2O_4$ NFs with different magnifications. From the panoramic image shown in Fig. 2a, it was observed that the sample was composed of a large number of nanoflakes. All these nanoflakes had a rectangle-like shape, and each flake was about 3.1 μm in length and 1.9 μm in width (Fig. 2b and c). The magnified SEM image in Fig. 2d further indicated the presence of many pores in the flake. In order to investigate the elemental
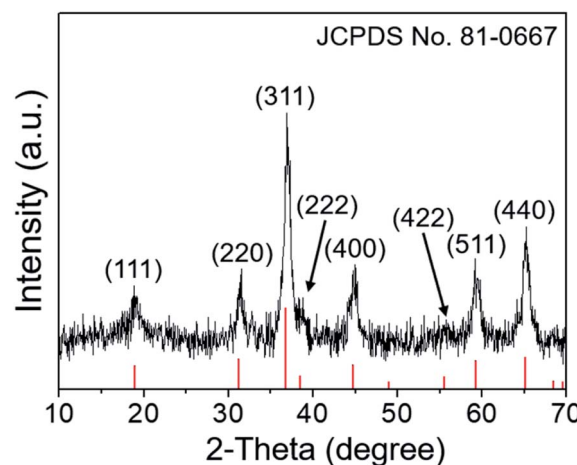

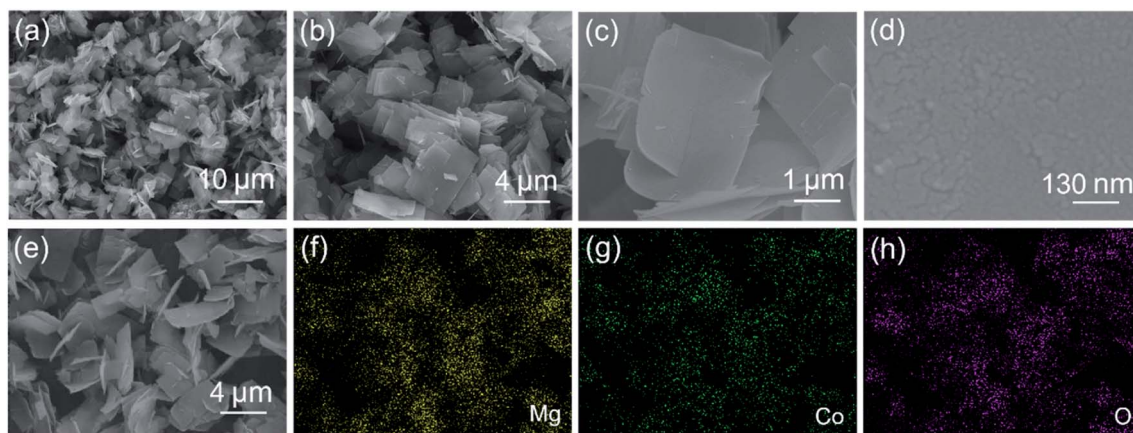Fig. 1 The XRD pattern of the porous $MgCo_2O_4$ nanoflakes obtained in the typical synthesis.

Fig. 2 (a–d) SEM images of $MgCo_2O_4$ NFs obtained in the typical synthesis with a post annealing process in air, and (e–h) SEM image of $MgCo_2O_4$ NFs and the corresponding elemental mapping images of Mg, Co, and O elements, respectively.

composition and distribution, the SEM image and its corresponding elemental mapping images were obtained and are shown in Fig. 2e–h. The similar shape of the mapping images suggested that elemental Mg, Co, and O were uniformly distributed throughout the flakes.

The detailed microstructure of $MgCo_2O_4$ NFs was further examined by TEM, and Fig. 3a shows a typical TEM image that was taken from the corner position of an arbitrarily selected flake. It directly indicated that the $MgCo_2O_4$ NF was actually composed of numerous NPs along with many pores. The porous structure was formed during the calcination process due to the decomposition of the precursor. The selected-area electron diffraction (SAED) pattern of the porous $MgCo_2O_4$ NF is shown in Fig. 3b; several ED rings can be clearly observed, suggesting the polycrystalline characteristic of the $MgCo_2O_4$ flake. The ED

rings can be indexed to the (111), (220), (311), (400), and (422) crystal planes of $MgCo_2O_4$, respectively, and match well with the XRD data. Fig. 3c shows a high-resolution TEM (HRTEM) image of the $MgCo_2O_4$ NF, from which the lattice can be clearly seen with regular orientations. Fig. 3d and e present the magnified HRTEM images of the circled positions in Fig. 3c, and the lattice spacings were calculated to be 0.24 and 0.20 nm, corresponding to the (311) and (400) lattice planes of cubic $MgCo_2O_4$, respectively.

The chemical composition and elemental valence states of $MgCo_2O_4$ NFs were investigated by XPS measurements. The peak of C 1s located at 284.6 eV was used as a reference to calibrate all the XPS spectra in this work. The full survey spectrum is illustrated in Fig. 4a, and the peaks indicating the presence of Mg, Co, O, and C elements can be clearly observed. The high resolution spectrum of Mg 1s is shown in Fig. 4b; it can be seen that the peak was located at about 1303 eV, suggesting the existence of Mg^{2+} in the $MgCo_2O_4$ NFs.[29] Fig. 4c displays the Co 2p XPS spectrum, and the two main peaks were centered at binding energies of 779.9 and 794.9 eV, corresponding to the Co $2p_{3/2}$ and Co $2p_{1/2}$, respectively.[32] The energy separation between the two main peaks was 15.0 eV, suggesting the presence of Co^{3+} in the $MgCo_2O_4$ NFs.[33] After Gaussian fitting, the two main peaks could be separated into two spin–orbit doublets, suggesting the coexistence of Co^{2+} and Co^{3+} in the sample. The peaks at binding energies of 779.4 and 794.4 eV corresponded to Co^{3+}, and the other two peaks at binding energies of 780.8 and 796.0 eV were ascribed to Co^{2+}.[34,35] Furthermore, two weak peaks at 786.7 and 803.2 eV could be identified as satellite peaks (marked as "Sat."), and were consistent with previously reported data.[36] Fig. 4d presents the high resolution spectrum of O 1s, and two fitting peaks were located at binding energies of 529.3 eV (O1) and 531.2 eV (O2), respectively. The peak at 529.3 eV was ascribed to metal–oxygen (Mg–O and Co–O) bonds and another one at 531.2 eV was attributed to the –OH group.[37,38]

Time-dependent experiments were conducted to investigate the shape evolution process of these $MgCo_2O_4$ NFs. In the first 2 h of hydrothermal reaction, the product was mainly composed
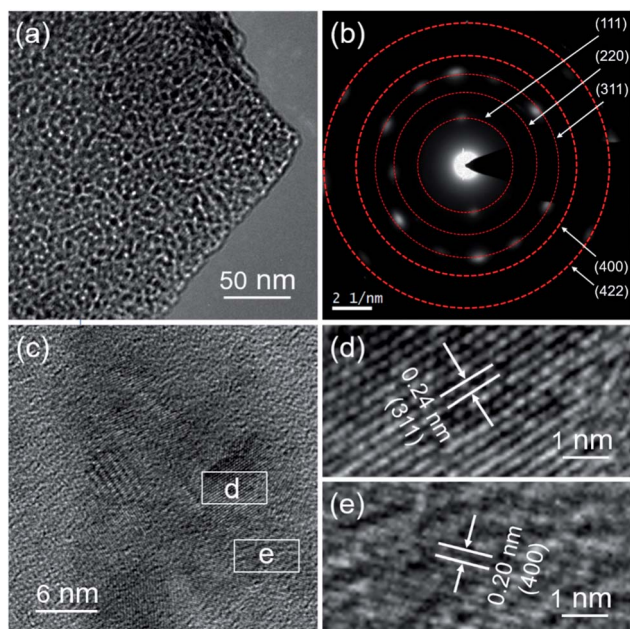

Fig. 3 (a) TEM image, (b) SAED pattern, (c) HRTEM image, and (d and e) magnified HRTEM images of the $MgCo_2O_4$ NFs.
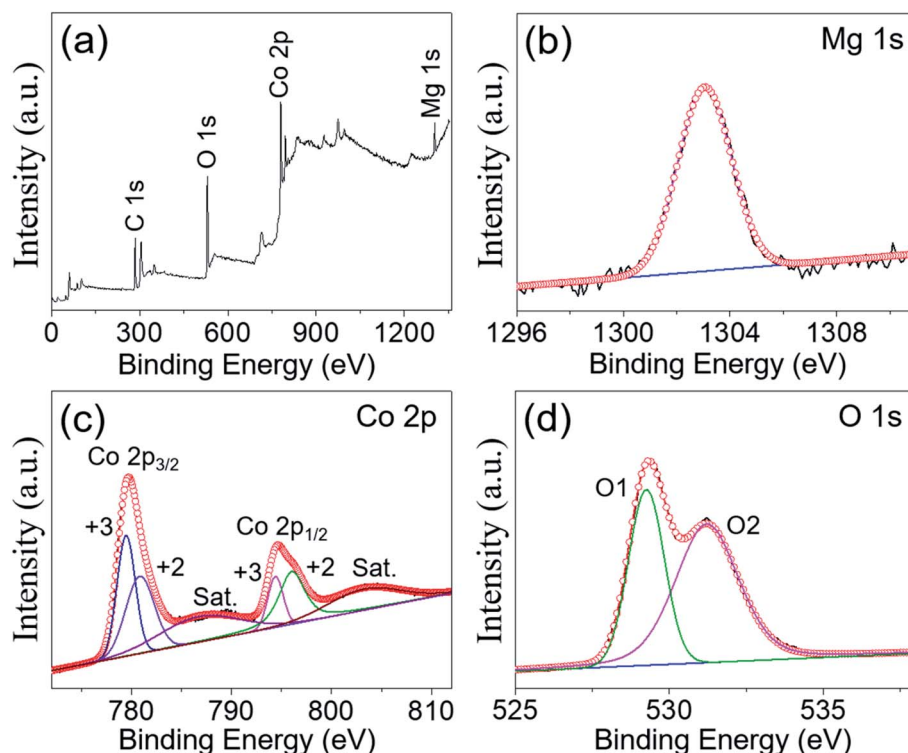
Fig. 4 (a) XPS survey spectrum and high-resolution spectra for (b) Mg 1s, (c) Co 2p, and (d) O 1s of the $MgCo_2O_4$ NFs.

of an urchin-like microstructure, which was constructed from many nanorods (Fig. 5a). As the reaction proceeded for 6 h, some of these nanorod-based urchin-like microstructures were transformed into thin nanoflakes (Fig. 5b). After 10 h, the sample was dominated by all the flakes, and the urchins completely disappeared. If the duration of hydrothermal reaction was continuously prolonged to 15 h, some flakes tended to be stacked and formed a loosely layered structure in order that the total surface free energy could be decreased (Fig. 5c). After that, the shape of $MgCo_2O_4$ had no obvious change even when

the reaction time was prolonged to 24 h, as revealed by the SEM image in Fig. 5d. Based on the above SEM observations, the formation process of $MgCo_2O_4$ NFs was believed to follow a typical Ostwald ripening mechanism. Nanoparticles (NPs) with a small size precipitated out at the initial stage, and these NPs could serve as seeds for the growth of the urchin-like structure or flakes in the following steps. The $MgCo_2O_4$ microstructures with a larger size were formed at the expense of the small particles. The detailed growth mechanism needs more investigation, and some related work is currently underway.

It was also found that temperature played an important role in the formation of $MgCo_2O_4$ NFs. Some samples were prepared at 105, 135, and 150 °C for 10 h while other procedures and parameters were the same. At low temperatures of 105 and 120 °C, $MgCo_2O_4$ flakes were produced as the dominant structure in the final sample (Fig. 6a and 2a). As the temperature increased to 135 °C, the total number of flakes reduced and few layered cubes coexisted (Fig. 6b). The reaction accelerated greatly at higher temperature, and more energy could be provided for the chemical reactions. When the temperature was high enough, the microstructures with less anisotropic shape would be formed finally due to the fast crystal growth. To obtain anisotropic microstructures, the temperature should be low and the nucleation step should be separated from the subsequent crystal growth step. So if the temperature was further increased to 150 °C, a huge quantity of less anisotropic quasi-cubes with an average edge length of about 7 μm were formed (Fig. 6c). The magnified SEM images in Fig. 6d and e indicated that the nanocubes (NCs) were also assembled with many NPs, and so the NCs exhibited a porous structure. The XRD pattern of the
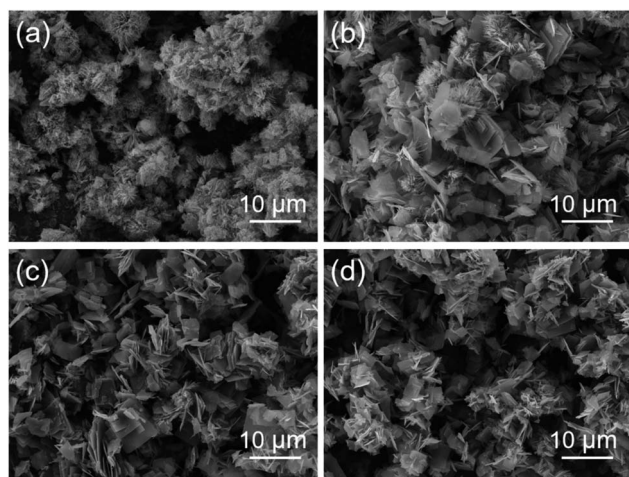

Fig. 5 SEM images of the $MgCo_2O_4$ samples prepared with hydrothermal reaction durations of (a) 2, (b) 6, (c) 15, and (d) 24 h, respectively. All the samples were annealed at 400 °C for 3 h.
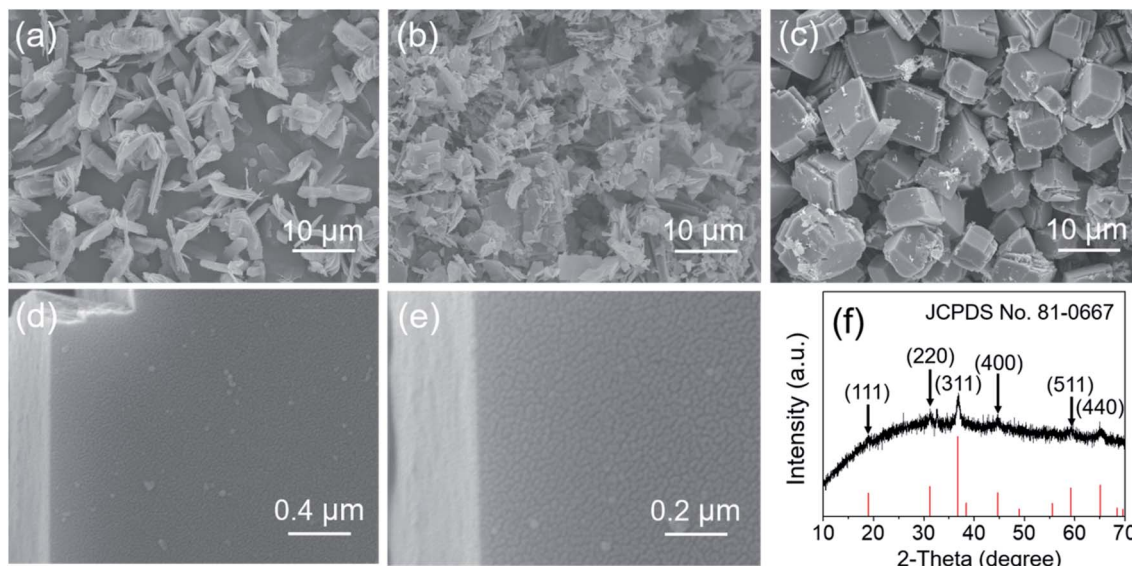
Fig. 6 SEM image of the MgCo$_2$O$_4$ samples prepared at (a) 105, (b) 135, and (c–e) 150 °C, respectively, and (f) the XRD pattern of the MgCo$_2$O$_4$ cubes. All the samples were annealed at 400 °C for 3 h.

MgCo$_2$O$_4$ NCs is presented in Fig. 6f. All the diffraction peaks can be well indexed to the cubic spinel structure of MgCo$_2$O$_4$ (JCPDS no. 81-0667), suggesting high purity of the obtained MgCo$_2$O$_4$ NCs.

A large specific surface area of an electrode material is one of the most important factors influencing its electrochemical performances. N$_2$ adsorption–desorption measurement was performed at 77 K to determine the specific surface area of MgCo$_2$O$_4$ NFs and NCs. The adsorption–desorption isotherms

of MgCo$_2$O$_4$ NFs are illustrated in Fig. 7a, and the isotherms could be classified as typical type-IV with a type H3 hysteresis, suggesting the mesoporous structure of MgCo$_2$O$_4$ NFs.[39] The specific surface area of MgCo$_2$O$_4$ NFs was calculated to be 64.9 m^2 g^{-1}, which was larger than that of a double-urchin-like MgCo$_2$O$_4$ hierarchical structure (26.45 m^2 g^{-1})[26] and flower-like MgCo$_2$O$_4$ microstructure (55 m^2 g^{-1}).[40] A porous structure with a large specific surface area is beneficial for the ion diffusion, and may enhance the electrochemical performances of an
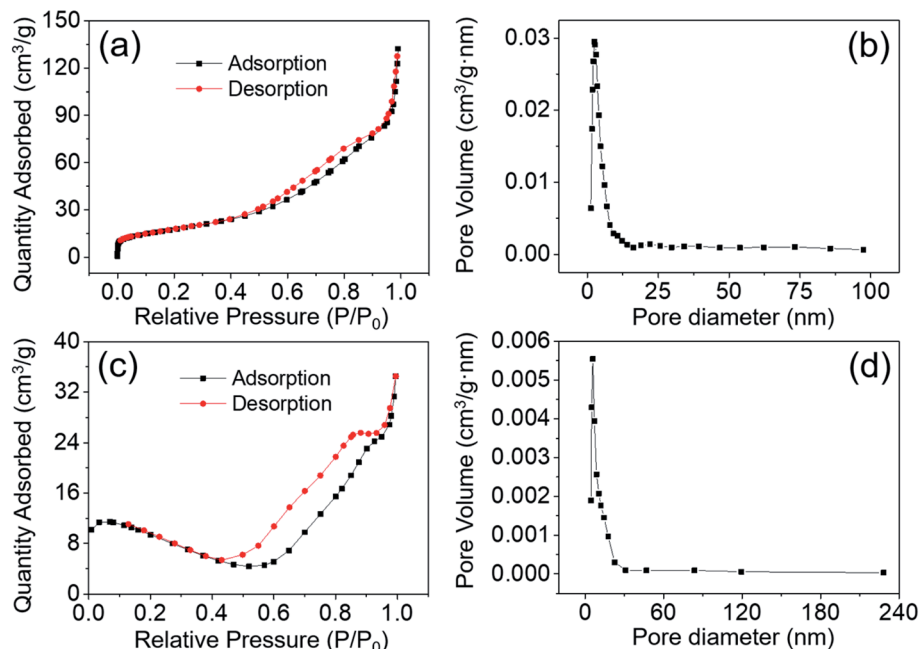

Fig. 7 Nitrogen adsorption–desorption isotherms and the corresponding BJH pore-size distribution plots of (a and b) the MgCo$_2$O$_4$ NFs and (c and d) the MgCo$_2$O$_4$ NCs, respectively.

electrode material. Fig. 7b reveals the pore size distribution of $MgCo_2O_4$ NFs using the BJH model. The pore size was mainly distributed at 2.8 nm and the average pore size was calculated to be 12.5 nm, further proving that the $MgCo_2O_4$ NFs possessed mesoporous features. For comparison, the specific surface area and pore size of $MgCo_2O_4$ NCs were also investigated, and the results are presented in Fig. 7c and d. The $MgCo_2O_4$ NCs exhibited a mesoporous characteristic with an average pore size of 9.8 nm, but the BET specific surface area was only 19.8 m^2 g^{-1}, far lower than that of $MgCo_2O_4$ NFs. It is widely known that the mesoporous structure is beneficial for the transportation of both electrons and ions, and full contact between the electrode material and electrolyte can promote the faradaic reactions. Furthermore, more actives sites can be provided by an electrode material with a larger specific surface area, so when used for supercapacitors, the $MgCo_2O_4$ NFs are expected to exhibit better electrochemical performance than $MgCo_2O_4$ NCs.

Based on the above discussion, the $MgCo_2O_4$ NFs may serve as a promising electrode material for supercapacitors, so the electrochemical performance is evaluated by cyclic voltammetry (CV), galvanostatic charge–discharge (GCD), electrochemical impedance spectroscopy (EIS), and cycling measurements. All the tests were conducted in a typical three-electrode system at room temperature and 2 M KOH aqueous solution was used as the electrolyte. As shown in Fig. 8a, several CV curves of the $MgCo_2O_4$ NF-modified electrode were obtained over a potential window of 0–0.6 V as the scan rates varied from 5 to 50 mV s^{-1}. Unlike the rectangular CV curves for electric double-layer capacitors, a couple of redox peaks can be observed in each CV curve, demonstrating the pseudo-capacitive behavior of $MgCo_2O_4$ NFs. The occurrence of redox peaks can be ascribed to the following reversible faradaic reactions:[29,41]

$$MgCo_2O_4 + 2H_2O \leftrightarrow 2CoOOH + Mg^{2+} + 2OH^- \quad (4)$$

$$CoOOH + H_2O + e^- \leftrightarrow Co(OH)_2 + OH^- \quad (5)$$

It was noticed that the anodic and cathodic peaks moved towards more positive and negative directions when the scan rate increased, which was attributed to the polarization and ohmic internal resistance of the electrode material.[42] The position of oxidation peaks moved from 0.34 to 0.47 V and the reduction peaks shifted from 0.19 to 0.12 V as the scan rate increased from 5 to 50 mV s^{-1}. The active sites at the inner surface of the electrode material cannot fully participate in the redox reactions because of the limited ion diffusion at high scan rate. Basically, all the CV curves obtained at different scan rates retained a symmetrical shape, indicating the excellent reversibility of the redox reactions taking place in the $MgCo_2O_4$ NF-based electrode.

The GCD tests were performed over a potential window of 0–0.43 V with the current density increasing from 1 to 12 A g^{-1}. As shown in Fig. 8b, the platforms on all the discharge curves can be clearly observed, suggesting the pseudo-capacitive characteristic of $MgCo_2O_4$ NFs. It is worth mentioning that the charge and discharge curves in all GCD curves at different current densities are symmetrical, indicating the high stability and coulombic efficiency of $MgCo_2O_4$ NFs. According to eqn (1), the specific capacitances were calculated to be 734.1, 670.7, 633.3, 590.1, 568.5, and 543.4 F g^{-1} at current densities of 1, 3, 5, 8, 10, and 12 A g^{-1}, respectively. The rate capability of $MgCo_2O_4$ NFs was about 74.0% as the current density increased from 1 to 12 A g^{-1}, suggesting a considerable rate performance. The specific capacitance decreased gradually with the increase of
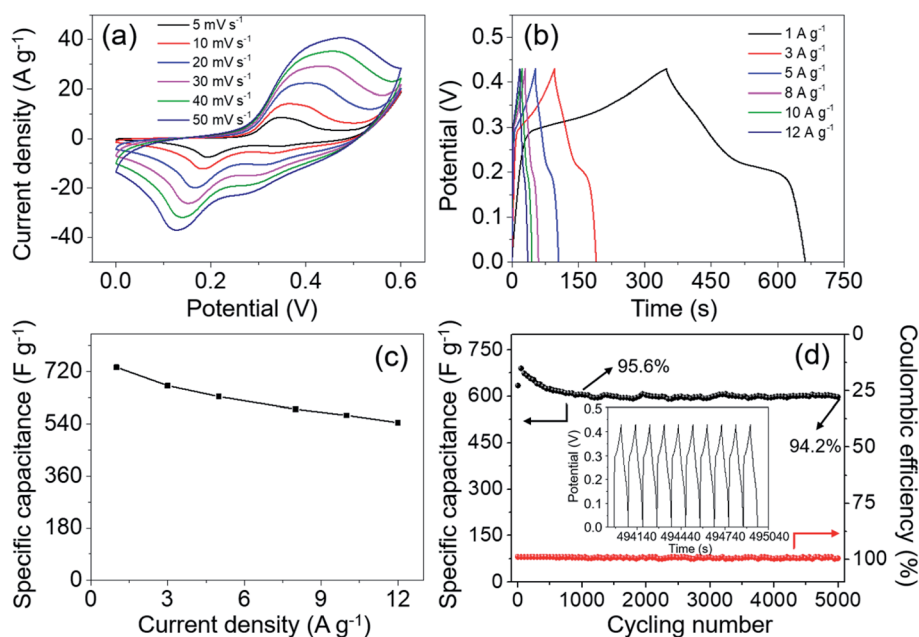

Fig. 8 Electrochemical tests of the $MgCo_2O_4$-NFs-modified electrode in 2 M KOH solution: (a) CV curves obtained at scan rates from 5 to 50 mV s^{-1}, (b) GCD curves measured at different current densities from 1 to 12 A g^{-1}, (c) specific capacitance at different current densities, and (d) cycling performance and coulombic efficiency at 5 A g^{-1} for 5000 cycles with the inset showing the last 10 cycles.

current density, which was directly observed from the curve of specific capacitance *vs.* current density in Fig. 8c. It demonstrated that the kinetics of redox reactions was mainly dominated by ion diffusion in the electrolyte. The use of PVDF binder and conductive carbon lead to a worse voltage drop at high current density, resulting in a decrease in specific capacitance. The capacitance value (734.1 F g^{-1} at 1 A g^{-1}) of MgCo$_2$O$_4$ NFs was higher than that of MgCo$_2$O$_4$ powder (321 F g^{-1} at 0.5 A g^{-1}),[24] double-urchin like MgCo$_2$O$_4$ microstructure (508 F g^{-1} at 2 A g^{-1}),[26] and MgCo$_2$O$_4$ twinned-hemispheres (626.5 F g^{-1} at 1 A g^{-1}).[43] It is no doubt that the electrode materials obtained using a binder-free method or BTMO-based composites usually exhibit better electrochemical performances. For instance, MgCo$_2$O$_4$ nanoneedle arrays directly grown on Ni foam delivered a specific capacitance of 804 F g^{-1} at a current density of 1 A g^{-1},[44] and MgCo$_2$O$_4$@MnO$_2$ core–shell arrays on graphene-coated Ni foam delivered a specific capacitance of 887.3 F g^{-1} at 1 A g^{-1}.[45] Considering the mass production and simple synthetic process, the MgCo$_2$O$_4$ NFs have considerable advantages as a promising electrode material for practical applications in supercapacitors.

Cycling stability is another important issue for an electrode material. Especially, a material with long-term cycling durability probably has a greater likelihood of being considered and used in supercapacitor devices. Hence, the cycling performance of MgCo$_2$O$_4$ NFs was evaluated through a continuous 5000 cycle GCD test at a constant current density of 5 A g^{-1}, and the result is shown in Fig. 8d. About 95.6% of the initial capacitance was retained after 1000 cycles, and at the end of the 5000th cycle, about 94.2% of the initial value was retained, suggesting the

excellent cycling performance of MgCo$_2$O$_4$ NFs. The electrochemical reversibility and cycling stability of electrode materials is also reflected by coulombic efficiency to some extent, which can be calculated from the following equation:

$$\eta = \frac{t_d}{t_c} \times 100\% \qquad (6)$$

where η represents the coulombic efficiency, and t_d and t_c are the discharge and charge times, respectively. The value of η was close to 100% during the whole 5000 cycle process, which suggested the good reversibility of faradaic reactions (Fig. 8d). In addition, the last 10 cycles are presented in the inset of Fig. 8d, from which a highly symmetric and linear shape with relatively small resistance drops can be observed, and it further confirmed the good electrochemical reversibility of the MgCo$_2$O$_4$ NF-modified electrode. After cycling, the MgCo$_2$O$_4$ NFs were examined by SEM and XRD (Fig. S2†), and the overall structure and shape of these NFs were well preserved (Fig. S2a†). It seemed that the surface of NFs became very rough, and it probably resulted from the continuous electron transfer and ion diffusion in the cycling process. The XRD data illustrated that the MgCo$_2$O$_4$ phase had almost no change (Fig. S2b†).

For comparison, the electrochemical performance of MgCo$_2$O$_4$ NCs was also investigated under the same test conditions. The CV test was performed over a potential window of 0–0.6 V. As the scan rate increased from 5 to 50 mV s^{-1}, all the CV curves exhibited similar shapes to those of the MgCo$_2$O$_4$ NF electrode (Fig. 9a). It also suggested that the MgCo$_2$O$_4$ NCs possessed pseudo-capacitance. Over a potential window of 0–0.43 V, the GCD curves were obtained at different current
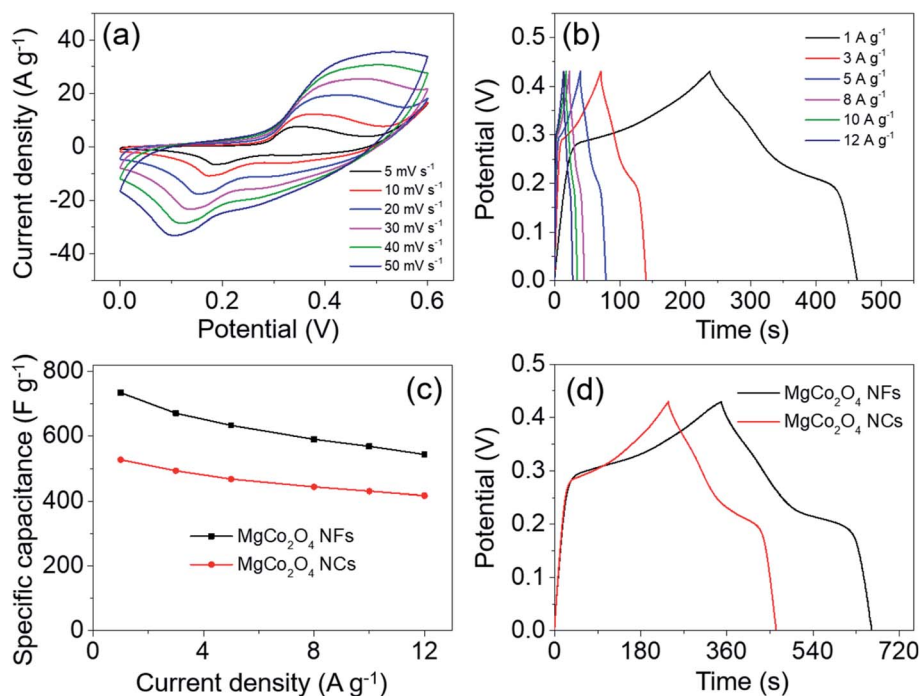

Fig. 9 (a) CV curves of MgCo$_2$O$_4$ NCs obtained at scan rates from 5 to 50 mV s^{-1}, (b) GCD curves of MgCo$_2$O$_4$ NCs measured at different current densities from 1 to 12 A g^{-1}, (c) the plot of specific capacitance *vs.* current density for MgCo$_2$O$_4$ NFs and MgCo$_2$O$_4$ NCs, respectively, and (d) GCD curves at 1 A g^{-1} for MgCo$_2$O$_4$ NFs and MgCo$_2$O$_4$ NCs, respectively. All the tests were performed in 2 M KOH aqueous electrolyte.
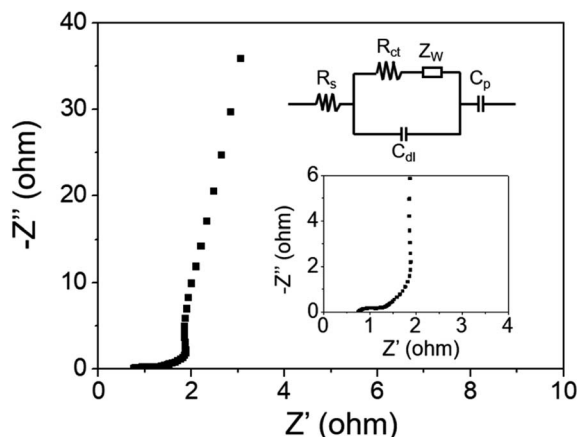
Fig. 10 Nyquist plot of the MgCo$_2$O$_4$-NF-modified electrode and the inset is the enlarged plot in the high frequency region as well as the corresponding equivalent circuit.

densities of 1–12 A g^{-1} (Fig. 9b). It can be clearly observed that the shape of these curves had no significant difference from that of MgCo$_2$O$_4$ NFs. The specific capacitances were calculated to be 541.0, 509.4, 488.1, 464.4, 452.5, and 440.9 F g^{-1} at current densities of 1, 3, 5, 8, 10, and 12 A g^{-1}, respectively, which were indeed lower than those of MgCo$_2$O$_4$ NFs (Fig. 9c). The rate capability of MgCo$_2$O$_4$ NCs was about 81.5% as the current density increased from 1 to 12 A g^{-1}. The GCD curves of MgCo$_2$O$_4$ NFs and NCs at the same current density of 1 A g^{-1} are shown in Fig. 9d, and it clearly demonstrated that the MgCo$_2$O$_4$ NFs delivered higher specific capacitance at 1 A g^{-1} due to the longer discharge time. The MgCo$_2$O$_4$ NFs possess larger specific surface area than NCs, and may provide more active sites for faradaic reactions. In addition, the ion diffusion and electron transfer can proceed more easily in the thin NFs than in the NCs, and so the inner impedance may be smaller for NFs. This probably is the basic reason that MgCo$_2$O$_4$ NFs deliver higher specific capacitance than the NCs.

The electrochemical impedance spectroscopy (EIS) test was conducted over the frequency range from 10^5 Hz to 10^{-2} Hz under open-circuit potential to explore the electrical conductivity of the MgCo$_2$O$_4$ NF electrode. The Nyquist plot is presented in Fig. 10, which consisted of a semicircle in the high frequency region and a straight line in the low frequency region. The value

of internal resistance (R_s) can be directly obtained from the intercept on the real axis (Z') at high frequency, which is the sum of ionic resistance of the electrolyte, intrinsic resistance of the material, and contact resistance between the electrode material and electrolyte.[46] R_{ct} indicates the charge transfer resistance during faradaic reactions, which can be represented by the diameter of the semicircle at high frequency. The slope of the straight line in the low frequency region is attributed to the Warburg impedance (Z_w), which is mainly produced from the diffusion resistance of OH$^-$ ions.[47] In this work, the values of R_s and R_{ct} were calculated to be 0.75 and 0.4 Ω, respectively. Such results suggest that the MgCo$_2$O$_4$ NF-based electrode possesses excellent electrical conductivity, and can serve as a promising electrode material for next-generation advanced supercapacitors.

In order to evaluate the practical applications of such MgCo$_2$O$_4$ NFs in supercapacitors, we fabricated an asymmetrical supercapacitor (ASC) device using MgCo$_2$O$_4$ NFs as a positive electrode and activated carbon (AC) as a negative electrode (MgCo$_2$O$_4$ NFs//AC ASC). Fig. S3† presents the electrochemical performances of the AC electrode, which was tested in 2 M KOH aqueous solution at room temperature. The specific capacitances of the AC electrode were calculated from GCD curves, and the values were 174.9, 168.2, 162.7, 160.4, 158.4, and 156.9 F g^{-1} at current densities of 1, 2, 4, 6, 8, and 10 A g^{-1}, respectively. It demonstrates that AC is an excellent negative electrode material for supercapacitors. It is worth noting that the positive and negative electrodes should satisfy the charge balance ($q^+ = q^-$), and then the ASC may achieve optimal performances. Several CV curves of the MgCo$_2$O$_4$ NFs//AC ASC obtained at a scan rate of 10 mV s^{-1} with different voltage windows are shown in Fig. 11a, and it is obvious that the operation voltage of such ASC could be enlarged to 0–1.7 V. It is well known that a larger voltage window may lead to higher energy density. In order to further confirm that this voltage window is appropriate, GCD tests were performed with different voltage windows at a current density of 1 A g^{-1} (Fig. 11b), and the voltage window of 0–1.7 V was found to be the most suitable for the ASC. The specific capacitances calculated from GCD curves with different voltage windows are shown in Fig. 11c. As the voltage window was enlarged from 0–1.0 to 0–1.7 V, the specific capacitance increased from 43.4 to 82.2 F g^{-1} and the energy density accordingly improved from 6.0 to 33.0 W h kg^{-1}. Hence, the appropriate voltage window for the electrochemical tests of the MgCo$_2$O$_4$ NFs//AC ASC is 0–1.7 V.
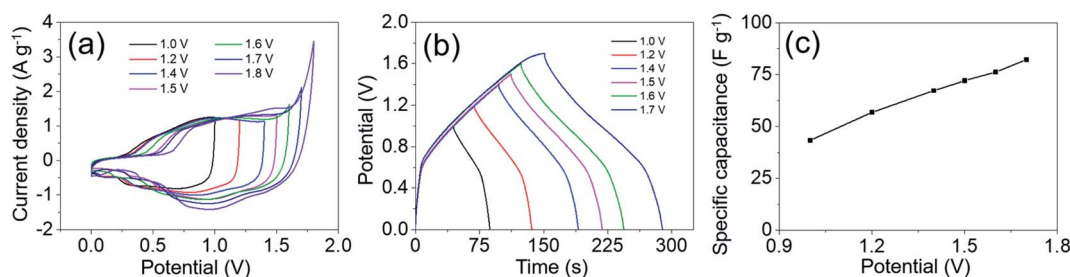

Fig. 11 (a) CV curves of the MgCo$_2$O$_4$ NFs//AC ASC measured over different voltage windows at a scan rate of 10 mV s^{-1}, (b) GCD curves of the MgCo$_2$O$_4$ NFs//AC ASC measured over different voltage windows at a current density of 1 A g^{-1}, and (c) specific capacitance as a function of voltage windows.

Fig. 12a shows the CV curves of the MgCo$_2$O$_4$ NFs//AC ASC that were obtained with scan rate increasing from 5 to 50 mV s^{-1} in the voltage window of 0–1.7 V. The distorted and rectangular shape of all the curves illustrated that both the pseudo-capacitance from MgCo$_2$O$_4$ NFs and the electric double-layer capacitance from AC contributed to the total capacitance of the ASC. The GCD curves obtained at different current densities (1–10 A g^{-1}) are presented in Fig. 12b, and the specific capacitances were calculated to be 82.2, 74.4, 68.5, 65.0, 63.3, and 61.5 F g^{-1} at 1, 2, 4, 6, 8, and 10 A g^{-1}, respectively (Fig. 12c). The capacitance retention was about 74.8% as the current density increased from 1 to 10 A g^{-1}, suggesting a good rate capability of the MgCo$_2$O$_4$ NFs//AC ASC. The MgCo$_2$O$_4$ NCs//AC ASC was also fabricated through the same procedure using MgCo$_2$O$_4$ NCs and AC as the positive and negative electrodes, respectively, and its electrochemical performance was evaluated under the same conditions. As shown in Fig. 12d and e, the CV and GCD curves suggested that the pseudo-capacitance of MgCo$_2$O$_4$ NCs and the electrode double-layer capacitance of the AC electrode also contributed to the capacitance of the MgCo$_2$O$_4$ NCs//AC ASC. The specific capacitances were calculated from the GCD curves and are shown in Fig. 12f. The values were 70.2, 68.5, 64.1, 63.2, 62.0, and 61.3 F g^{-1} at 1, 2, 4, 6, 8, and 10 A g^{-1}, respectively, which were lower than those of the MgCo$_2$O$_4$ NFs//AC ASC. From the above analysis, it can be concluded that the MgCo$_2$O$_4$ NFs possess better electrochemical properties and may have great potential for supercapacitors.

The long-term cycling stability is also important for the ASC device. The cycling performances of the MgCo$_2$O$_4$ NFs//AC ASC and MgCo$_2$O$_4$ NCs//AC ASC were evaluated at a current density of 5 A g^{-1}, and the results are shown in Fig. 13. After a continuous 4000 cycle GCD process, the capacitance of the MgCo$_2$O$_4$ NFs//AC ASC maintained approximately 110.4% of its initial value, and the coulombic efficiency remained at almost 100% during the whole cycling process (Fig. 13a). The last 5 GCD curves are displayed in Fig. 13b, and the shape of the curves had no significant change and remained symmetrical. It suggested the excellent cycling performance of the MgCo$_2$O$_4$ NFs//AC ASC. As shown in Fig. 13c, the capacitance retention of the MgCo$_2$O$_4$ NCs//AC ASC was about 104.8% after 4000 cycles, and the coulombic efficiency also remained close to 100%. The last 5 GCD curves shown in Fig. 13d also had a symmetrical shape.

Energy and power densities are vital factors in determining the practical applications of supercapacitors; in this case, the energy and power densities of the MgCo$_2$O$_4$ NFs//AC ASC as well as the MgCo$_2$O$_4$ NCs//AC ASC were calculated based on GCD curves, and the Ragone plot is illustrated in Fig. 14. The MgCo$_2$O$_4$ NFs//AC ASC exhibited an energy density of 33.0 W h kg^{-1} at a power density of 859.6 W kg^{-1}, and retained 24.7 W h kg^{-1} when the power density increased to 9527.6 W kg^{-1}. In comparison, the MgCo$_2$O$_4$ NCs//AC ASC exhibited an energy density of 28.2 W h kg^{-1} at a power density of 860.4 W kg^{-1}. The energy density of the MgCo$_2$O$_4$ NFs//AC ASC is higher than those of several previously reported ASCs based on MgCo$_2$O$_4$ or other TMOs, such as NiCo$_2$O$_4$ nanosheets/CuCo$_2$O$_4$ nanocones/NF//AC (15 W h kg^{-1} at 814 W kg^{-1}),[48] NiCo$_2$S$_4$ NPs// AC (28.3 W h kg^{-1} at 245 W kg^{-1}),[39] MgCo$_2$O$_4$ nanosheets/NF// AC (12.99 W h kg^{-1} at 448.7 W kg^{-1}),[42] and Co$_3$O$_4$/NF//carbon
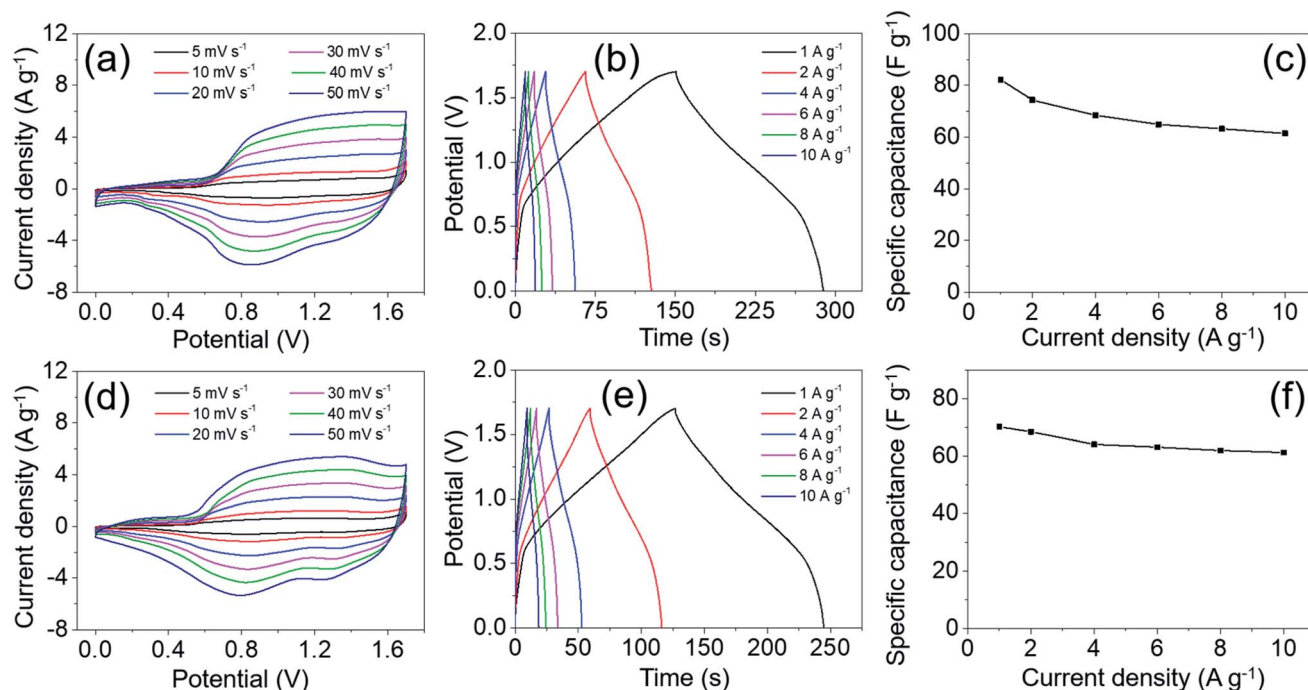

Fig. 12 Electrochemical tests for the MgCo$_2$O$_4$ NFs//AC ASC in 2 M KOH solution: (a) CV curves at different scan rates in the voltage window of 0–1.7 V, (b) GCD curves at different current densities, and (c) the specific capacitance at various current densities. Electrochemical tests for the MgCo$_2$O$_4$ NCs//AC ASC: (d) CV curves at different scan rates in the voltage window of 0–1.7 V, (e) GCD curves at different current densities, and (f) the specific capacitance at various current densities.
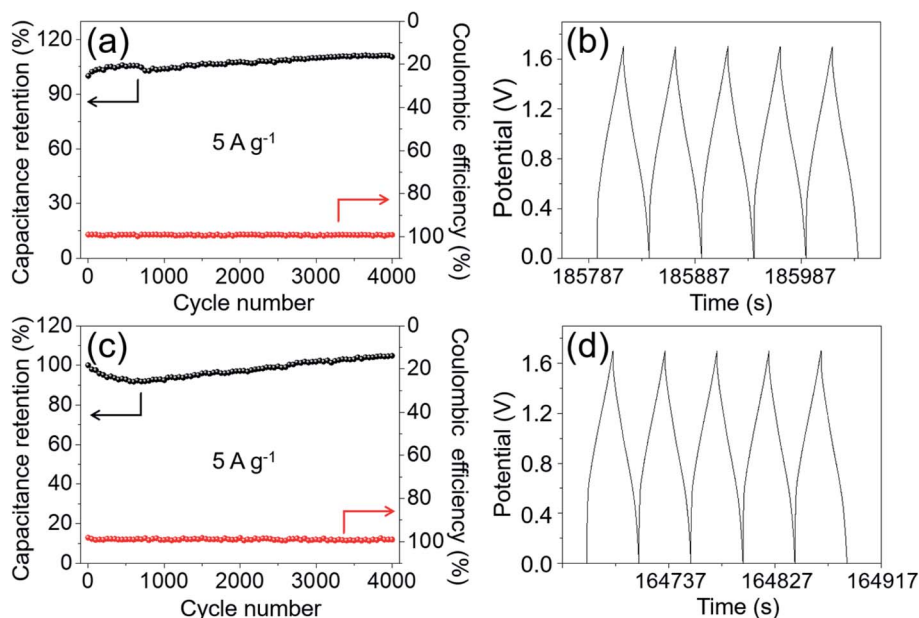
Fig. 13 (a) Consecutive 4000 cycle GCD curves at 5 A g^{-1} and the related coulombic efficiency, and (b) the last 5 GCD curves of the MgCo$_2$O$_4$ NFs//AC ASC, (c) continuous 4000 cycle GCD curves at 5 A g^{-1} and the related coulombic efficiency, and (d) the last 5 GCD curves of the MgCo$_2$O$_4$ NCs//AC ASC.

aerogel microspheres (17.9 W h kg^{-1} at 750 W kg^{-1}).[49] However, these values are still lower than those of some composites or other cobalt-based oxides directly grown on conductive substrates, such as urchin-like MgCo$_2$O$_4$@ppy/NF//AC (33.4 W h kg^{-1} at 320 W kg^{-1}),[29] double-urchin-like hierarchical MgCo$_2$O$_4$@NiMo$_2$O$_4$ core–shell nanomaterial/NF//AC (37.5 W h kg^{-1} at 480 W kg^{-1}),[30] ZnCo$_2$O$_4$ NW cluster arrays/NF//AC (41 W h kg^{-1} at 384 W kg^{-1}),[50] and MgCo$_2$O$_4$ nanoneedles/NF//rGO (81 W h kg^{-1} at 1350 W kg^{-1}).[44] From the viewpoint of large-scale synthesis of powdered electrode materials and low cost, the MgCo$_2$O$_4$ NFs//AC ASC fabricated in this work achieves a wide operation voltage of 0–1.7 V and delivers an energy density as high as 33.0 W h kg^{-1}, and all the results

indicate that the MgCo$_2$O$_4$ NFs can be considered as a promising electrode material for supercapacitors.

4. Conclusions

In summary, MgCo$_2$O$_4$ nanoflakes with a rectangular shape were successfully synthesized *via* a hydrothermal method followed by an annealing treatment of the precursor. These MgCo$_2$O$_4$ NFs have a mesoporous structure with an average pore diameter of 12.5 nm and a specific surface area up to 64.9 m^2 g^{-1}. The electrode modified with MgCo$_2$O$_4$ NFs delivered a specific capacitance of 734.1 F g^{-1} at 1 A g^{-1} and 543.4 F g^{-1} at 12 A g^{-1}. After 5000 cycles at 5 A g^{-1}, the specific capacitance remained at about 94.2% of its initial value, suggesting a superior cycling stability of such electrode. In addition, the MgCo$_2$O$_4$ NFs//AC ASC delivered an energy density of 33.0 W h kg^{-1} at a power density of 859.6 W kg^{-1}. Such ASC also exhibited excellent cycling performance, and almost 110.4% of the original capacitance was retained after 4000 cycles at a current density of 5 A g^{-1}. All the results illustrate that the MgCo$_2$O$_4$ NFs have superior electrochemical performance and great application potential as an electrode material for supercapacitors.

Conflicts of interest

There are no conflicts to declare.

Acknowledgements

Fig. 14 Ragone plots of the MgCo$_2$O$_4$ NFs//AC ASC, MgCo$_2$O$_4$ NCs//AC ASC and other ASCs reported previously.

References

1 L. Yu, B. Guan, W. Xiao and X. W. Lou, Formation of yolk-shelled Ni-Co mixed oxide nanoprisms with enhanced electrochemical performance for hybrid supercapacitors and lithium ion batteries, *Adv. Energy Mater.*, 2015, **5**, 1500981.

2 Y. Ouyang, H. Ye, X. Xia, X. Jiao, G. Li, S. Mutahir, L. Wang, D. Mandler, W. Lei and Q. Hao, Hierarchical electrodes of $NiCo_2S_4$ nanosheets-anchored sulfur-doped Co_3O_4 nanoneedles with advanced performance for battery-supercapacitor hybrid devices, *J. Mater. Chem. A*, 2019, **7**, 3228–3237.

3 F. Liao, X. Han, Y. Zhang, X. Han, C. Xu and H. Chen, Hydrothermal synthesis of mesoporous $MnCo_2O_4/CoCo_2O_4$ ellipsoid-like microstructures for high-performance electrochemical supercapacitors, *Ceram. Int.*, 2019, **45**, 7244–7252.

4 B. Y. Guan, A. Kushima, L. Yu, S. Li, J. Li and X. W. Lou, Coordination polymers derived general synthesis of multishelled mixed metal-oxide particles for hybrid supercapacitors, *Adv. Mater.*, 2017, **29**, 1605902.

5 F. Lai, J. Feng, T. Heil, Z. Tian, J. Schmidt, G.-C. Wang and M. Oschatz, Partially delocalized charge in Fe-doped $NiCo_2S_4$ nanosheet-mesoporous carbon-composites for high-voltage supercapacitors, *J. Mater. Chem. A*, 2019, **7**, 19342–19347.

6 H. Chen, X. Du, J. Sun, Y. Wang, Y. Zhang and C. Xu, Solvothermal synthesis of novel pod-like $MnCo_2O_{4.5}$ microstructures as high-performance electrode materials for supercapacitors, *Int. J. Hydrogen Energy*, 2019, 3016–3027.

7 S. Li, Y. Wang, J. Sun, Y. Zhang, C. Xu and H. Chen, Hydrothermal synthesis of Fe-doped Co_3O_4 urchin-like microstructures with superior electrochemical performances, *J. Alloys Compd.*, 2020, **821**, 153507.

8 Z. Yu, L. Tetard, L. Zhai and J. Thomas, Supercapacitor electrode materials: nanostructures from 0 to 3 dimensions, *Energy Environ. Sci.*, 2015, **8**, 702–730.

9 Y. Wang, S. Li, J. Sun, Y. Zhang, H. Chen and C. Xu, Simple solvothermal synthesis of magnesium cobaltite microflowers as a battery grade material with high electrochemical performances, *Ceram. Int.*, 2019, **45**, 14642–14651.

10 Q. F. Wang, X. F. Wang, B. Liu, G. Yu, X. J. Hou, D. Chen and G. Z. Shen, $NiCo_2O_4$ nanowire arrays supported on Ni foam for high-performance flexible all-solid-state supercapacitors, *J. Mater. Chem. A*, 2013, **1**, 2468–2473.

11 Q. Wang, L. Zhu, L. Sun, Y. Liu and L. Jiao, Facile synthesis of hierarchical porous $ZnCo_2O_4$ microspheres for high-performance supercapacitors, *J. Mater. Chem. A*, 2015, **3**, 982–985.

12 L. Xu, Y. Zhao, J. Lian, Y. Xu, J. Bao, J. Qiu, L. Xu, H. Xu, M. Hua and H. Li, Morphology controlled preparation of $ZnCo_2O_4$ nanostructures for asymmetric supercapacitor with ultrahigh energy density, *Energy*, 2017, **123**, 296–304.

13 G. M. Tomboc, H. S. Jadhav and H. Kim, PVP assisted morphology-controlled synthesis of hierarchical mesoporous $ZnCo_2O_4$ nanoparticles for high-performance pseudocapacitor, *Chem. Eng. J.*, 2017, **308**, 202–213.

14 Y. Teng, Y. Li, Z. Zhang, D. Yu, Y. Feng, Y. Meng, W. Tong, Y. Wu, X. Zhao and X. Liu, One-step controllable synthesis of mesoporous $MgCo_2O_4$ nanosheet arrays with ethanol on nickel foam as an advanced electrode material for high-performance supercapacitors, *Chemistry*, 2018, **24**, 14982–14988.

15 F. Liao, X. Han, D. Cheng, Y. Zhang, X. Han, C. Xu and H. Chen, MnO_2 hierarchical microspheres assembled from porous nanoplates for high-performance supercapacitors, *Ceram. Int.*, 2019, **45**, 1058–1066.

16 J. Sun, Y. Wang, Y. Zhang, C. Xu and H. Chen, Egg albumin-assisted hydrothermal synthesis of Co_3O_4 quasi-cubes as superior electrode material for supercapacitors with excellent performances, *Nanoscale Res. Lett.*, 2019, **14**, 340.

17 V. S. Kumbhar and D. H. Kim, Hierarchical coating of MnO_2 nanosheets on $ZnCo_2O_4$ nanoflakes for enhanced electrochemical performance of asymmetric supercapacitors, *Electrochim. Acta*, 2018, **271**, 284–296.

18 F. Liao, X. Han, Y. Zhang, C. Xu and H. Chen, Solvothermal synthesis of porous $MnCo_2O_{4.5}$ spindle-like microstructures as high-performance electrode materials for supercapacitors, *Ceram. Int.*, 2018, **44**, 22622–22631.

19 C. H. An, Y. J. Wang, Y. N. Huang, Y. N. Xu, L. F. Jiao and H. T. Yuan, Porous $NiCo_2O_4$ nanostructures for high performance supercapacitors *via* a microemulsion technique, *Nano Energy*, 2014, **10**, 125–134.

20 J. Cheng, Y. Lu, K. Qiu, H. Yan, X. Hou, J. Xu, L. Han, X. Liu, J. K. Kim and Y. Luo, Mesoporous $ZnCo_2O_4$ nanoflakes grown on nickel foam as electrodes for high performance supercapacitors, *Phys. Chem. Chem. Phys.*, 2015, **17**, 17016–17022.

21 H. Gao, Y. Li, H. Zhao, J. Xiang and Y. Cao, A general fabrication approach on spinel MCo_2O_4 (M = Co, Mn, Fe, Mg and Zn) submicron prisms as advanced positive materials for supercapacitor, *Electrochim. Acta*, 2018, **262**, 241–251.

22 X. Guan, Q. Wang, P. Luo, Y. Yu, X. Li, Y. Zhang and D. Chen, Morphology-tuned synthesis of $MgCo_2O_4$ arrays on graphene coated nickel foam for high-rate supercapacitor electrode, *Int. J. Electrochem. Sci.*, 2018, **13**, 2272–2285.

23 M. Kim and J. Kim, Redox active KI solid-state electrolyte for battery-like electrochemical capacitive energy storage based on $MgCo_2O_4$ nanoneedles on porous β-polytype silicon carbide, *Electrochim. Acta*, 2018, **260**, 921–931.

24 S. G. Krishnan, M. V. Reddy, M. Harilal, B. Vidyadharan, I. I. Misnon, M. H. A. Rahim, J. Ismail and R. Jose, Characterization of $MgCo_2O_4$ as an electrode for high performance supercapacitors, *Electrochim. Acta*, 2015, **161**, 312–321.

25 S. G. Krishnan, M. Harilal, I. I. Misnon, M. V. Reddy, S. Adams and R. Jose, Effect of processing parameters on

the charge storage properties of MgCo$_2$O$_4$ electrodes, *Ceram. Int.*, 2017, **43**, 12270–12279.

26 J. Xu, L. Wang, J. Zhang, J. Qian, J. Liu, Z. Zhang, H. Zhang and X. Liu, Fabrication of porous double-urchin-like MgCo$_2$O$_4$ hierarchical architectures for high-rate supercapacitors, *J. Alloys Compd.*, 2016, **688**, 933–938.

27 X. Wu, L. Meng, Q. Wang, W. Zhang and Y. Wang, A high performance asymmetric supercapacitor based on carbon fiber coated with MgCo$_2$O$_4$ nanobrush, *Mater. Lett.*, 2017, **206**, 71–74.

28 L. Cui, L. Huang, M. Ji, Y. Wang, H. Shi, Y. Zuo and S. Kang, High-performance MgCo$_2$O$_4$ nanocone arrays grown on three-dimensional nickel foams: preparation and application as binder-free electrode for pseudo-supercapacitor, *J. Power Sources*, 2016, **333**, 118–124.

29 H. Gao, X. Wang, G. Wang, C. Hao, S. Zhou and C. Huang, An urchin-like MgCo$_2$O$_4$@PPy core-shell composite grown on Ni foam for a high-performance all-solid-state asymmetric supercapacitor, *Nanoscale*, 2018, **10**, 10190–10202.

30 H. Gao, X. Wang, G. Wang, C. Hao, C. Huang and C. Jiang, Facile construction of a MgCo$_2$O$_4$@NiMoO$_4$/NF core-shell nanocomposite for high-performance asymmetric supercapacitors, *J. Mater. Chem. C*, 2019, **7**, 13267–13278.

31 H. Shin and W. J. Lee, Multi-shelled MgCo$_2$O$_4$ hollow microspheres as anodes for lithium ion batteries, *J. Mater. Chem. A*, 2016, **4**, 12263–12272.

32 F. X. Bao, X. F. Wang, X. D. Zhao, Y. Wang, Y. Ji, H. D. Zhang and X. Y. Liu, Controlled growth of mesoporous ZnCo$_2$O$_4$ nanosheet arrays on Ni foam as high-rate electrodes for supercapacitors, *RSC Adv.*, 2014, **4**, 2393–2397.

33 B. Fan, X. Chen, A. Hu, Q. Tang, H. Fan, Z. Liu and K. Xiao, Facile synthesis of 3D plum candy-like ZnCo$_2$O$_4$ microspheres as a high-performance anode for lithium ion batteries, *RSC Adv.*, 2016, **6**, 79971–79977.

34 H. Yan, Y. Lu, K. Zhu, T. Peng, X. Liu, Y. Liu and Y. Luo, Growth of highly mesoporous CuCo$_2$O$_4$@C core-shell arrays as advanced electrodes for high-performance supercapacitors, *Appl. Surf. Sci.*, 2018, **439**, 883–890.

35 X. Han, F. Liao, Y. Zhang, H. Chen and C. Xu, Template-free synthesis of mesoporous ZnCo$_2$O$_4$ nanosheets and quasi-cubes *via* a simple solvothermal route, *Mater. Lett.*, 2018, **217**, 56–59.

36 B. Liu, H. Liu, M. Liang, L. Liu, Z. Lv, H. Zhou and H. Guo, Controlled synthesis of hollow octahedral ZnCo$_2$O$_4$ nanocages assembled from ultrathin 2D nanosheets for enhanced lithium storage, *Nanoscale*, 2017, **9**, 17174–17180.

37 X. Y. Zhou, G. H. Chen, J. J. Tang, Y. P. Ren and J. Yang, One-dimensional NiCo$_2$O$_4$ nanowire arrays grown on nickel foam for high-performance lithium-ion batteries, *J. Power Sources*, 2015, **299**, 97–103.

38 S. Liu, K. San Hui, K. N. Hui, J. M. Yun and K. H. Kim, Vertically stacked bilayer CuCo$_2$O$_4$/MnCo$_2$O$_4$ heterostructures on functionalized graphite paper for high-

performance electrochemical capacitors, *J. Mater. Chem. A*, 2016, **4**, 8061–8071.

39 Y. R. Zhu, Z. B. Wu, M. J. Jing, X. M. Yang, W. X. Song and X. B. Ji, Mesoporous NiCo$_2$S$_4$ nanoparticles as high-performance electrode materials for supercapacitors, *J. Power Sources*, 2015, **273**, 584–590.

40 S. G. Krishnan, M. Harilal, A. Yar, B. L. Vijayan, J. O. Dennis, M. M. Yusoff and R. Jose, Critical influence of reduced graphene oxide mediated binding of M (M = Mg, Mn) with Co ions, chemical stability and charge storability enhancements of spinal-type hierarchical MCo$_2$O$_4$ nanostructures, *Electrochim. Acta*, 2017, **243**, 119–128.

41 H. Chen, J. Wang, X. Han, F. Liao, Y. Zhang, L. Gao and C. Xu, Facile synthesis of mesoporous ZnCo$_2$O$_4$ hierarchical microspheres and their excellent supercapacitor performance, *Ceram. Int.*, 2019, **45**, 8577–8584.

42 S. Vijayakumar, S. Nagamuthu and K. S. Ryu, In situ preparation of MgCo$_2$O$_4$ nanosheets on Ni-foam as a binder-free electrode for high performance hybrid supercapacitors, *Dalton Trans.*, 2018, **47**, 6722–6728.

43 Y. Wang, X. Ma, S. Li, J. Sun, Y. Zhang, H. Chen and C. Xu, Facile solvothermal synthesis of novel MgCo$_2$O$_4$ twinned-hemispheres for high performance asymmetric supercapacitors, *J. Alloys Compd.*, 2019, 152905.

44 J. Xu, L. Wang, Y. Sun, J. Zhang, C. Zhang and M. Zhang, Fabrication of porous MgCo$_2$O$_4$ nanoneedle arrays/Ni foam as an advanced electrode material for asymmetric supercapacitors, *J. Alloys Compd.*, 2019, **779**, 100–107.

45 X. Guan, P. Luo, X. Li, Y. Yu, Y. Wang, L. Zhuo and D. Chen, Magnesium cobaltate nanowires@magnanese dioxide nanoflakes core-shell arrays on graphene-decorated nickel foam for high-performance supercapacitors, *Int. J. Electrochem. Sci.*, 2018, **13**, 5016–5030.

46 H. Chen, J. Wang, F. Liao, X. Han, C. Xu and Y. Zhang, Facile synthesis of porous Mn-doped Co$_3$O$_4$ oblique prisms as an electrode material with remarkable pseudocapacitance, *Ceram. Int.*, 2019, **45**, 8008–8016.

47 M. Cheng, H. Fan, Y. Song, Y. Cui and R. Wang, Interconnected hierarchical NiCo$_2$O$_4$ microspheres as high-performance electrode materials for supercapacitors, *Dalton Trans.*, 2017, **46**, 9201–9209.

48 S. Wen, Y. Liu, H. Bai, R. Shao, W. Xu and W. Shi, Full synergistic effect of hydrothermal NiCo$_2$O$_4$ nanosheets/CuCo$_2$O$_4$ nanocones supported on Ni foam for high-performance asymmetric supercapacitors, *J. Solid State Chem.*, 2018, **262**, 327–334.

49 W. Liu, X. Li, M. Zhu and X. He, High-performance all-solid state asymmetric supercapacitor based on Co$_3$O$_4$ nanowires and carbon aerogel, *J. Power Sources*, 2015, **282**, 179–186.

50 B. Guan, D. Guo, L. Hu, G. Zhang, T. Fu, W. Ren, J. Li and Q. Li, Facile synthesis of ZnCo$_2$O$_4$ nanowire cluster arrays on Ni foam for high-performance asymmetric supercapacitors, *J. Mater. Chem. A*, 2014, **2**, 16116–16123.